Energy-Efficient Coordinated Torque Distribution Control for Stability of Hub Motor Electric Vehicles

Guanyue Zhang, Zixu Zhao, Chunguang Liu*
Department of Weaponry and Control, Army Academy of Armored Forces, Beijing, China
**Corresponding Author*

Abstract: An energy-efficient torque allocation strategy is developed for four-wheel independently driven electric vehicles, with both handling stability and in-wheel motor efficiency incorporated into a unified framework. A two-level control structure is designed for this purpose. At the supervisory level, a two-degree-of-freedom vehicle model is used to predict vehicle motion, while model predictive control determines the corrective yaw moment through receding-horizon calculations. Meanwhile, the overall longitudinal force requirement is derived from the driver's input. At the allocation level, the wheel torque distribution problem is formulated as a convex quadratic program subject to linear equality and boundary constraints. The objective function considers both tire-force utilization and motor power dissipation, and the resulting optimization problem is solved online using an interior-point algorithm. An adaptive weighting strategy based on phase-plane characteristics is further introduced to balance vehicle stability and energy efficiency under different operating conditions. Moreover, an anti-slip function is embedded in the lower-level controller. By continuously monitoring wheel slip ratios and adjusting the corresponding wheel torques, the proposed controller suppresses excessive wheel slip and improves driving safety and stability on low-adhesion roads.

Keywords: Hub-Motor Drive; Torque Distribution; Quadratic Programming; Tire Adhesion Utilization; Motor Power Loss; Anti-Slip Regulation

1. Introduction

Mounting a traction machine inside each wheel hub removes the kinematic coupling that differentials and half-shafts impose, so four torque channels become individually addressable. The redundancy is attractive—longitudinal and yaw demands can be served at once with no additional hardware—but it leaves an ill-posed decision: infinitely many torque quadruples reproduce the same pair of generalised commands [1]. Selecting one of them is the allocation problem treated below.

Yaw motion is corrected by deliberately unbalancing the left- and right-hand longitudinal forces, an intervention usually labelled direct yaw-moment control. Because the plant owns more inputs than controlled directions, the customary remedy is to split the design: a motion layer settles the generalised force and moment, and an allocation layer maps them onto the actuators [2, 3].

For the motion layer, proportional–integral–derivative regulators, sliding-mode laws and finite-horizon optimal laws have all been reported. Feedback torque-vectoring architectures have been benchmarked against one another, and sliding-mode variants—non-singular terminal forms in particular—are favoured whenever parameter drift and unmodelled disturbance dominate [4]. A single-input single-output formulation that regulates yaw rate and sideslip angle concurrently has also been demonstrated [5]. Finite-horizon optimal control remains the most frequently adopted option, chiefly because actuator saturation and rate limits enter the formulation explicitly rather than through ad-hoc clipping [6]; reported variants address real-time yaw-motion optimisation [7], combined longitudinal–lateral regulation and stability recovery near the friction limit [8], while reference generation and safe following additionally depend on how road geometry and comfort limits are encoded [9].

For the allocation layer, the dominant cost is the squared friction exploitation of the four contacts, whose minimisation enlarges the distance to saturation [10]. Machine efficiency, however, varies steeply with the operating point, and a cost blind to that map keeps part of the drives in low-efficiency territory throughout a manoeuvre. Consumption-oriented splits and multi-objective formulations that weigh economy against handling have therefore appeared [3]. Two questions are still open. First, the trade-off is normally frozen at design time, whereas the appropriate emphasis clearly depends on how close the vehicle currently is to instability. Second, allocation feasibility is asserted through a friction bound that relies on an estimated μ; when the estimate lags a surface transition, the commanded torque exceeds what the contact can transmit and the driven wheels spin.

Three contributions follow from these observations. (i) The corrective yaw moment is obtained from an incremental finite-horizon optimisation built on a steer-angle-dependent 2-DOF predictor, so that offset-free tracking and explicit moment rate limits are obtained simultaneously. (ii) The allocation cost couples a quadratic friction term with a linear dissipation term whose coefficients are read from the measured efficiency map, and the two are blended by a factor derived analytically from the phase-plane distance, which removes the torque discontinuities produced by hard mode switching. (iii) A spin-limiting stage with equal-per-axle torque reduction is appended, which restores robustness against μ mis-estimation while leaving the left–right torque difference—hence the delivered yaw moment—untouched.

Section 2 fixes the architecture and the models, Sections 3 and 4 develop the two layers, Section 5 reports the co-simulation evidence and Section 6 concludes.

2. Hierarchical Control Architecture and Basic Models

2.1 Overall Hierarchical Control Architecture

Stability regulation together with torque partitioning of the distributed-drive electric vehicle is handled here by a two-level controller, the overall arrangement being given in Figure 1. Two blocks make up that arrangement, referred to below as the upper-layer and the lower-layer controller.

Direct yaw-moment regulation is carried out in the upper layer. Taking a 2-DOF vehicle description as its predictor, a model predictive law is re-solved at each sampling instant and delivers the additional yaw moment ΔM_z, whereas the total traction demand F_x never enters that law and is instead read off the accelerator-pedal signal. Two modules follow in the lower layer, one performing torque distribution and one limiting wheel spin. Within the distribution module, F_x and ΔM_z handed down from above are imposed as equalities; the torque of every wheel is bounded in addition by what the machine can deliver at its present speed and by what the road contact is able to transmit; a quadratic program then picks the four-wheel torques, its cost weighing tyre adhesion utilization against power loss of the hub machines. What leaves the distribution module is not issued directly but screened by the anti-slip module: slip of each driven wheel is followed in real time, and a wheel whose slip passes the preset threshold has its torque capped or pulled back, so that excessive spin is avoided and the driving force actually reaches the road. Acting as the plant is the full vehicle dynamics model, whose returned state variables reach the upper layer and close the loop.

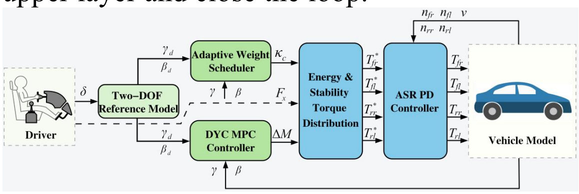

Figure 1. Overall Architecture of the Hierarchical Control System

2.2 2-DOF Vehicle Reference Model

Vehicle sideslip angle β and yaw rate γ are selected as the principal variables for evaluating vehicle stability. To generate the reference signals required by the supervisory controller, a linear two-degree-of-freedom vehicle model is established, as illustrated in Figure 2.

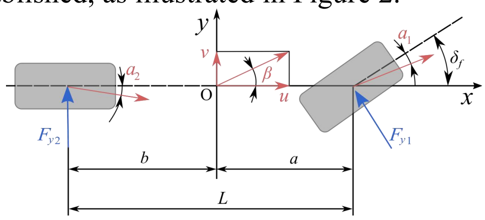

Figure 2. Diagram of the Two-Degree-of-Freedom Vehicle Model

To simplify the vehicle dynamics, the following assumptions are introduced:

a) Steering-system dynamics are omitted. Accordingly, the front-wheel steering angle δ_f is treated as the direct control input and is

assumed to remain sufficiently small;
b) Rolling resistance, road gradient resistance, and aerodynamic drag are not considered;
c) Roll, pitch, and heave motions of the vehicle body are ignored;
d) Tire transient characteristics are neglected, and the tires are assumed to operate within their linear-force range.

Under these assumptions, the state-space representation of the 2-DOF model can be written as

$$\begin{bmatrix} \dot{\beta} \\ \dot{\gamma} \end{bmatrix} = \boldsymbol{A} \begin{bmatrix} \beta \\ \gamma \end{bmatrix} + \boldsymbol{B}\, \delta_f \tag{1}$$

where β is the sideslip angle; γ represents the yaw rate; δ_f is the steering angle of the front wheels; Matrices $\boldsymbol{A}$ and $\boldsymbol{B}$ are the state and input matrices. The tire lateral force adopts a linear cornering model and satisfies the self-aligning convention $F_y = -C\alpha$, thereby ensuring that the trace of the system state matrix is negative at normal vehicle speeds and that the vehicle is open-loop stable. The two matrices are, respectively:

$$\boldsymbol{A} = \begin{bmatrix} a_{11} & a_{12} \\ a_{21} & a_{22} \end{bmatrix} = \begin{bmatrix} -\dfrac{C_f + C_r}{mv} & -\dfrac{aC_f - bC_r}{mv^2} - 1 \\ -\dfrac{aC_f - bC_r}{I_z} & -\dfrac{a^2 C_f + b^2 C_r}{I_z v} \end{bmatrix} \tag{2}$$

$$\boldsymbol{B} = \begin{bmatrix} b_{11} \\ b_{21} \end{bmatrix} = \begin{bmatrix} \dfrac{C_f}{mv} \\ \dfrac{aC_f}{I_z} \end{bmatrix} \tag{3}$$

Here, C_f and C_r are the cornering stiffnesses of the front and rear tires. Parameters a and b denote the longitudinal distances from the vehicle center of mass to the front and rear axles, respectively. Furthermore, I_z is the vehicle yaw moment of inertia, m is the total vehicle mass, and v represents the longitudinal velocity.

By imposing the steady-state condition on the state equation, the desired yaw rate and sideslip angle are derived as

$$\begin{cases} \gamma_d^* = \dfrac{v}{(1+Kv^2)L}\delta_f \\ \beta_d^* = \dfrac{b/L - mav^2/(L^2 C_r)}{1+Kv^2}\delta_f \end{cases} \tag{4}$$

where γ_d^* and β_d^* denote the steady-state reference values of yaw rate and sideslip angle, respectively. The parameter L is the wheelbase, while the stability factor K is defined as $K = \dfrac{m}{L^2}\dfrac{bC_r - aC_f}{C_f C_r}$.

Because the achievable lateral response is restricted by the available tire–road friction, the reference yaw rate and sideslip angle must satisfy

$$|\, a_y| \le \mu g \tag{5}$$

where a_y is the lateral acceleration, μ denotes the tire–road adhesion coefficient, and g is gravitational acceleration.

To improve vehicle adaptability under varying road conditions and prevent an excessive sideslip response, the final reference values are determined as:

$$\begin{cases} \gamma_d = \min\left[|\, \gamma_d^*|, \left| \dfrac{0.85\mu g}{v} \right| \right] \operatorname{sgn}(\delta_f) \\ \beta_d = 0 \end{cases} \tag{6}$$

where γ_d and β_d represent the ideal yaw rate and sideslip angle after constraint correction, respectively, while $\operatorname{sgn}(\cdot)$ denotes the signum function.

2.3 In-Wheel Motor Model

The energy dissipation of each in-wheel motor is formulated as:

$$P_{loss,i} = \begin{cases} T_i \omega_i \left(\dfrac{1}{\eta(T_i, \omega_i)} - 1 \right), T_i > 0 \\ T_i \omega_i \left(\eta(T_i, \omega_i) - 1 \right), T_i \le 0 \end{cases} \tag{7}$$

where $P_{loss,i}$ represents the power dissipated by the i-th in-wheel motor; T_i and ω_i denote its driving torque and angular velocity, respectively; and $\eta(T_i, \omega_i)$ is the motor efficiency corresponding to the current torque and speed. The efficiency value can be determined from the experimentally obtained efficiency map and output characteristic curve. The subscript $i \in \{\text{fl}, \text{fr}, \text{rl}, \text{rr}\}$ identifies the front-left, front-right, rear-left, and rear-right wheels, respectively.

By defining the power-loss coefficient g_i, Eq. (7) can be rewritten in the following unified form:

$$P_{loss,i} = g_i\, T_i \tag{8}$$

where:

$$g_i = \begin{cases} \omega_i \left(\dfrac{1}{\eta_i} - 1 \right), T_i > 0 \\ \omega_i \left(\eta_i - 1 \right), T_i \le 0 \end{cases} \tag{9}$$

and $\eta_i = \eta(T_i, \omega_i)$ denotes the efficiency of the i-th motor at its present operating point, which is extracted from the motor efficiency map shown in Figure 3. When $T_i > 0$, the motor operates in the driving condition, $g_i > 0$, and the power loss $P_{loss,i} = g_i T_i > 0$; when $T_i \le 0$, the motor operates in the regenerative braking condition, $g_i < 0$, and after multiplication by the negative torque the power loss remains positive, which is physically consistent.

According to the output characteristic of the in-wheel motor, its maximum available torque is expressed as

$$T_{\max} = \begin{cases} T_{\max,peak}, 0 < n \le n_N \\ \dfrac{9550 P_{\max}}{n}, n_N < n < n_{\max} \end{cases} \tag{10}$$

where $T_{\max}$ is the maximum torque available at the current motor speed; $T_{\max,peak}$ denotes the peak torque within the constant-torque range; n is the motor rotational speed in r/min ; n_N and $n_{\max}$ are the rated and maximum motor speeds, respectively; and $P_{\max}$ represents the maximum motor power.

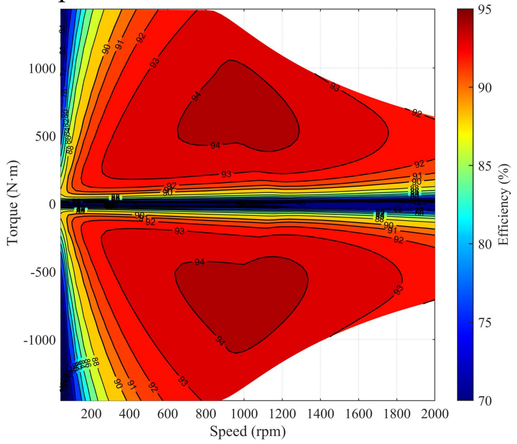

Figure 3. Efficiency Characteristics of the In-Wheel Motor

3. Design of the Upper-Layer Stability Controller

The supervisory controller adopts model predictive control (MPC) to calculate the corrective yaw moment ΔM_z in real time. Meanwhile, the required total longitudinal force F_x is determined directly from the driver's accelerator-pedal command. A 2-DOF vehicle model augmented with the corrective yaw moment is employed as the prediction model.

At each sampling instant, the MPC controller uses the measured vehicle states to predict the system response over a finite horizon. The optimal sequence of control increments is then obtained by solving a constrained quadratic programming problem. Only the first element of this sequence is implemented, after which the optimization procedure is repeated at the next sampling instant. In this way, the actual yaw rate and sideslip angle can accurately follow their desired values.

Compared with traditional PID control, MPC can explicitly handle the amplitude and rate constraints of the control variable, and improves the tracking accuracy and robustness with respect to the nonlinear vehicle dynamics through multi-step prediction and receding-horizon optimization.

3.1 Derivation of the Prediction Model

To achieve an appropriate trade-off between prediction accuracy and computational efficiency, an augmented two-degree-of-freedom vehicle model incorporating the corrective yaw moment is selected as the prediction model. Assuming a sufficiently small sideslip angle, i.e., $\beta \approx v_y/v$, the lateral and yaw dynamics can be described by the following nonlinear state equation $\dot{\boldsymbol{x}} = \boldsymbol{f}(\boldsymbol{x},u)$:

$$\begin{bmatrix} \dot{\beta} \\ \dot{\gamma} \end{bmatrix} = \begin{bmatrix} \dfrac{1}{mv}\left(F_{y1}\cos\delta_f + F_{y2}\right) - \gamma \\ \dfrac{1}{I_z}\left(aF_{y1}\cos\delta_f - bF_{y2} + \Delta M_z\right) \end{bmatrix} \tag{11}$$

where the state vector $\boldsymbol{x} = [\beta,\gamma]^{\mathrm{T}}$ and the control input $u = \Delta M_z$. The tire lateral force adopts the linear cornering model $F_{y1} = -C_f \alpha_1$ and $F_{y2} = -C_r \alpha_2$, and the front and rear tire slip angles, after the small-angle approximation, are:

$$\alpha_1 \approx \beta + \frac{a\gamma}{v} - \delta_f, \quad \alpha_2 \approx \beta - \frac{b\gamma}{v} \tag{12}$$

Substituting the linear tire-force expressions into Eq. (11) and rearranging the resulting equations yields a linearized state-space model. The front-wheel steering angle is assumed to remain unchanged throughout the prediction horizon and is regarded as a measurable disturbance, denoted by $w = \delta_f$. Thus, the model can be expressed as

$$\dot{\boldsymbol{x}} = \tilde{\boldsymbol{A}}\boldsymbol{x} + \tilde{\boldsymbol{B}}u + \boldsymbol{E}_c w \tag{13}$$

where the linearized state matrix is

$$\tilde{\boldsymbol{A}} = \begin{bmatrix} -\dfrac{C_f\cos\delta_f + C_r}{mv} & -\dfrac{aC_f\cos\delta_f - bC_r}{mv^2} - 1 \\ -\dfrac{aC_f\cos\delta_f - bC_r}{I_z} & -\dfrac{a^2C_f\cos\delta_f + b^2C_r}{I_z v} \end{bmatrix} \tag{14}$$

The control input matrix $\tilde{\boldsymbol{B}}$ and the front-wheel steering angle disturbance matrix $\boldsymbol{E}_c$ are, respectively:

$$\tilde{\boldsymbol{B}} = \begin{bmatrix} 0 \\ 1/I_z \end{bmatrix}, \quad \boldsymbol{E}_c = \begin{bmatrix} C_f\cos\delta_f/(mv) \\ aC_f\cos\delta_f/I_z \end{bmatrix} \tag{15}$$

When $\cos\delta_f \approx 1$, $\tilde{\boldsymbol{A}}$ degenerates into the reference model state matrix $\boldsymbol{A}$, and $\boldsymbol{E}_c$ degenerates into the input matrix $\boldsymbol{B}$, reflecting the inherent consistency between the prediction model and the reference model; retaining the $\cos\delta_f$ term gives the prediction model higher prediction accuracy under large steering-angle conditions.

3.2 Model Discretization and Incremental Formulation

Let T_s denote the MPC sampling interval. By applying the first-order Euler method and omitting the second- and higher-order terms, the continuous-time model is converted into the following discrete-time form:

$$\boldsymbol{x}(k+1) = \boldsymbol{A}_d\boldsymbol{x}(k) + \boldsymbol{B}_u u(k) + \boldsymbol{E}_d w \tag{16}$$

where

$$\boldsymbol{A}_d = e^{\tilde{A}T_s} \approx \boldsymbol{I} + \tilde{\boldsymbol{A}}T_s = \begin{bmatrix} \tilde{a}_{11}T_s + 1 & \tilde{a}_{12}T_s \\ \tilde{a}_{21}T_s & \tilde{a}_{22}T_s + 1 \end{bmatrix} \tag{17}$$

$$\boldsymbol{B}_u \approx T_s\tilde{\boldsymbol{B}} = \begin{bmatrix} 0 \\ T_s/I_z \end{bmatrix},\quad \boldsymbol{E}_d \approx T_s\boldsymbol{E}_c = \begin{bmatrix} C_f\cos\delta_f \cdot T_s/(mv) \\ aC_f\cos\delta_f \cdot T_s/I_z \end{bmatrix} \tag{18}$$

To enhance steady-state tracking and suppress residual tracking errors, the control input is reformulated in incremental form: $\Delta u(k) = u(k) - u(k-1)$, yielding:

$$\boldsymbol{x}(k+1) = \boldsymbol{A}_d\boldsymbol{x}(k) + \boldsymbol{B}_u u(k-1) + \boldsymbol{B}_u\Delta u(k) + \boldsymbol{E}_d w \tag{19}$$

Defining the augmented state vector $\boldsymbol{\xi}(k) = [\boldsymbol{x}(k)^{\mathrm{T}}, u(k-1)]^{\mathrm{T}} \in \mathbb{R}^3$, the augmented discrete state-space equation becomes:

$$\boldsymbol{\xi}(k+1) = \bar{\boldsymbol{A}}\boldsymbol{\xi}(k) + \bar{\boldsymbol{B}}\Delta u(k) + \bar{\boldsymbol{E}}w \tag{20}$$

$$\boldsymbol{y}(k) = \bar{\boldsymbol{C}}\boldsymbol{\xi}(k) \tag{21}$$

with the augmented system matrices:

$$\bar{\boldsymbol{A}} = \begin{bmatrix} \boldsymbol{A}_d & \boldsymbol{B}_u \\ \boldsymbol{0}_{1\times 2} & 1 \end{bmatrix}, \bar{\boldsymbol{B}} = \begin{bmatrix} \boldsymbol{B}_u \\ 1 \end{bmatrix}, \bar{\boldsymbol{E}} = \begin{bmatrix} \boldsymbol{E}_d \\ 0 \end{bmatrix}, \bar{\boldsymbol{C}} = [\boldsymbol{I}_2 \quad \boldsymbol{0}_{2\times 1}] \tag{22}$$

3.3 Construction of the Prediction Equation

Let N_p and N_c denote the prediction and control horizons, respectively, where $N_c \le N_p$. Beyond the control horizon, the control increment is assumed to be zero. The predicted output sequence over the entire prediction horizon can therefore be written as

$$\boldsymbol{Y}(k+1|\,k) = \boldsymbol{S}_\xi\boldsymbol{\xi}(k) + \boldsymbol{S}_u\Delta\boldsymbol{U}(k) + \boldsymbol{S}_w w \tag{23}$$

where $\boldsymbol{Y}(k+1|\,k) = [\boldsymbol{y}(k+1|\,k)^{\mathrm{T}}, \ldots, \boldsymbol{y}(k+N_p|\,k)^{\mathrm{T}}]^{\mathrm{T}} \in \mathbb{R}^{2N_p}$, $\Delta\boldsymbol{U}(k) = [\Delta u(k), \ldots, \Delta u(k+N_c-1)]^{\mathrm{T}} \in \mathbb{R}^{N_c}$ and the propagation matrices are:

$$\boldsymbol{S}_\xi = \begin{bmatrix} \bar{\boldsymbol{C}}\bar{\boldsymbol{A}} \\ \bar{\boldsymbol{C}}\bar{\boldsymbol{A}}^2 \\ \vdots \\ \bar{\boldsymbol{C}}\bar{\boldsymbol{A}}^{N_p} \end{bmatrix} \tag{24}$$

$$\boldsymbol{S}_u = \begin{bmatrix} \bar{\boldsymbol{C}}\bar{\boldsymbol{B}} & \boldsymbol{0} & \cdots & \boldsymbol{0} \\ \bar{\boldsymbol{C}}\bar{\boldsymbol{A}}\bar{\boldsymbol{B}} & \bar{\boldsymbol{C}}\bar{\boldsymbol{B}} & \cdots & \boldsymbol{0} \\ \vdots & \vdots & \ddots & \vdots \\ \bar{\boldsymbol{C}}\bar{\boldsymbol{A}}^{N_p-1}\bar{\boldsymbol{B}} & \bar{\boldsymbol{C}}\bar{\boldsymbol{A}}^{N_p-2}\bar{\boldsymbol{B}} & \cdots & \bar{\boldsymbol{C}}\bar{\boldsymbol{A}}^{N_p-N_c}\bar{\boldsymbol{B}} \end{bmatrix} \tag{25}$$

$$\boldsymbol{S}_w = \begin{bmatrix} \bar{\boldsymbol{C}}\bar{\boldsymbol{E}} \\ \sum_{i=0}^{1}\bar{\boldsymbol{C}}\bar{\boldsymbol{A}}^{i}\bar{\boldsymbol{E}} \\ \vdots \\ \sum_{i=0}^{N_p-1}\bar{\boldsymbol{C}}\bar{\boldsymbol{A}}^{i}\bar{\boldsymbol{E}} \end{bmatrix} \tag{26}$$

3.4 Formulation and Solution of the Optimization Problem

The desired yaw rate γ_d and sideslip angle β_d are combined to define the reference vector $\boldsymbol{r} = [\beta_d, \gamma_d]^{\mathrm{T}}$. The reference sequence is:

$$\boldsymbol{R}_k = [\boldsymbol{r}(k+1|\,k)^{\mathrm{T}}, \boldsymbol{r}(k+2|\,k)^{\mathrm{T}}, \ldots, \boldsymbol{r}(k+N_p|\,k)^{\mathrm{T}}]^{\mathrm{T}} \tag{27}$$

The optimization objective function is:

$$J = \left(\boldsymbol{Y} - \boldsymbol{R}_k\right)^{\mathrm{T}}\boldsymbol{Q}\left(\boldsymbol{Y} - \boldsymbol{R}_k\right) + \Delta\boldsymbol{U}^{\mathrm{T}}\boldsymbol{W}\Delta\boldsymbol{U} \tag{28}$$

where $\boldsymbol{Q} = \mathrm{diag}(q_1, q_2, \ldots, q_{2N_p}) \succeq 0$ and $\boldsymbol{W} = \mathrm{diag}(w_1, w_2, \ldots, w_{N_c}) \succ 0$.

After substitution and rearrangement:

$$J = \Delta\boldsymbol{U}^{\mathrm{T}}\underbrace{\left(\boldsymbol{S}_u^{\mathrm{T}}\boldsymbol{Q}\boldsymbol{S}_u + \boldsymbol{W}\right)}_{\mathrm{H}}\Delta\mathrm{U} + \underbrace{2\boldsymbol{\Phi}^{\mathrm{T}}\boldsymbol{Q}\boldsymbol{S}_u}_{\mathrm{F}^{\mathrm{T}}}\Delta\boldsymbol{U} + \boldsymbol{\Phi}^{\mathrm{T}}\boldsymbol{Q}\boldsymbol{\Phi} \tag{29}$$

(with the constant term omitted). The additional yaw moment must satisfy:

$$|\,\Delta u(k+i|\,k)| \le \Delta u_{\max},\quad i = 0,1,\ldots,N_c-1 \tag{30}$$

$$u_{\min} \le u(k+i|\,k) \le u_{\max},\quad i = 0,1,\ldots,N_c-1 \tag{31}$$

The quadratic programming problem solved at each sampling instant is:

$$\min_{\Delta\boldsymbol{U}}\ \Delta\boldsymbol{U}^{\mathrm{T}}\mathrm{H}\,\Delta\boldsymbol{U} + \mathrm{F}^{\mathrm{T}}\Delta\boldsymbol{U} \tag{32}$$

$$\text{s.t.}\quad \boldsymbol{A}_{ineq}\Delta\boldsymbol{U} \le \boldsymbol{b}_{ineq} \tag{33}$$

Following the receding-horizon principle, only the first component of the optimized control sequence is implemented. The corrective yaw moment is updated according to

$$\Delta M_z(k) = \Delta M_z(k-1) + \Delta u^*(k) \tag{34}$$

where $\Delta u^*(k)$ represents the first optimal control increment obtained at the current sampling instant.

4. Design of the Lower-layer Controller

The lower-level controller takes the required total longitudinal force F_x and the corrective yaw moment ΔM_z , generated by the upper-level controller, as its command inputs. These generalized force demands are allocated among the four in-wheel motors. An anti-slip strategy is subsequently used to examine and, when necessary, modify the resulting torque commands.

The lower-level control scheme contains two functional components: an optimal torque allocation module and an anti-slip control module. The former determines the four-wheel torque commands by solving a quadratic programming problem in which tire adhesion utilization and motor power dissipation are simultaneously considered. The latter checks the allocated torques and corrects them to prevent excessive drive-wheel slip.

4.1 Optimal Torque Distribution

4.1.1 Mapping of generalized forces and moments to wheel torques

The relationship between the generalized vehicle-force demand and the torque commands of the four wheels is given by:

$$\begin{cases} F_x = \frac{1}{R}\left(T_{fl}\cos\delta_f + T_{fr}\cos\delta_f + T_{rl} + T_{rr}\right) \\ \Delta M_z = \frac{1}{R}[\left(-\frac{c}{2}\cos\delta_f + a\sin\delta_f\right)T_{fl} \\ \quad +\left(\frac{c}{2}\cos\delta_f + a\sin\delta_f\right)T_{fr} - \frac{c}{2}T_{rl} + \frac{c}{2}T_{rr}. \end{cases} \tag{35}$$

Here, F_x denotes the resultant longitudinal driving force required from the four wheels. The variables T_{fl} , T_{fr} , T_{rl} , and T_{rr} are the torque commands of the front-left, front-right, rear-left, and rear-right wheels, respectively. Moreover, c is the vehicle track width, R is the effective rolling radius of the wheels, a denotes the longitudinal distance from the front axle to the vehicle center of mass, and δ_f is the front-wheel steering angle.

Equation (35) can be written compactly in matrix form as

$$\boldsymbol{v}_d = \boldsymbol{B}_d \boldsymbol{u}_d \tag{36}$$

where $\boldsymbol{v}_d = \begin{bmatrix} F_x & \Delta M_z \end{bmatrix}^{\mathrm{T}}$ is the generalized force-demand vector; F_x is the total demanded longitudinal force; $\boldsymbol{u}_d = \begin{bmatrix} T_{fl} & T_{fr} & T_{rl} & T_{rr} \end{bmatrix}^{\mathrm{T}}$ is the four-wheel torque distribution vector; and $\boldsymbol{B}_d$ is the moment mapping matrix:

$$\boldsymbol{B}_d = \frac{1}{R}\begin{bmatrix} \cos\delta_f & \cos\delta_f & 1 & 1 \\ -\frac{c}{2}\cos\delta_f + a\sin\delta_f & \frac{c}{2}\cos\delta_f + a\sin\delta_f & -\frac{c}{2} & \frac{c}{2} \end{bmatrix} \tag{37}$$

The first row of this mapping matrix indicates that the resultant of the driving forces of all wheels along the longitudinal axis equals the total demanded longitudinal force, and the second row describes the yaw moments generated by the four wheel forces about the vehicle's center of mass, whose sum must track the corrective yaw-moment command.

4.1.2 Objective function

Both vehicle handling stability and in-wheel motor energy efficiency are considered in the torque allocation process. Accordingly, the optimization criterion consists of two weighted components: tire adhesion utilization and total motor power dissipation.

Tire adhesion utilization reflects the proportion of the available tire–road friction capacity occupied by the longitudinal wheel force. A smaller value generally indicates a greater reserve of tire adhesion and, consequently, a larger vehicle stability margin. Because tire lateral forces are affected by vehicle velocity, steering angle, and vertical wheel load, they cannot be independently regulated through motor torque allocation. Therefore, only the longitudinal tire forces are included in the allocation objective.

The tire adhesion objective is constructed from the weighted sum of the squared adhesion-utilization ratios of the four wheels:

$$J_1 = \frac{1}{2}\boldsymbol{u}_d^{\mathrm{T}}\boldsymbol{H}\boldsymbol{u}_d \tag{38}$$

where J_1 is the tire adhesion utilization objective term; and $\boldsymbol{H}$ is a 4×4 positive-definite diagonal weight matrix:

$$\boldsymbol{H} = \mathrm{diag}\left(\frac{\sigma_i}{(\mu R F_{zi})^2}\right), \quad i \in \{\mathrm{fl, fr, rl, rr}\} \tag{39}$$

In Eq. (39), σ_i is the weighting coefficient assigned to the i -th wheel. Appropriately increasing the rear-wheel weights can help preserve vehicle handling stability. Moreover, μ represents the tire–road adhesion coefficient, F_{zi} is the vertical load acting on the i -th wheel, and R denotes the effective wheel rolling radius. Provided that $\sigma_i > 0$, matrix $\boldsymbol{H}$ is positive definite.

To improve the economy of the in-wheel motors, the sum of the power losses of all motors is taken as a linear objective term to reduce the total energy loss rate:

$$J_2 = \sum_{i=fl,fr,rl,rr} P_{loss,i} = \boldsymbol{G}^{\mathrm{T}}\boldsymbol{u}_d \tag{40}$$

where J_2 is the motor power loss objective term; $\boldsymbol{G} = \begin{bmatrix} g_{fl} & g_{fr} & g_{rl} & g_{rr} \end{bmatrix}^{\mathrm{T}}$ is the loss coefficient vector; and g_i is the loss coefficient of the i-th motor, whose definition is given in Eq. (9).

Combining the above two terms with weighting, the final optimization objective function is obtained:

$$\min J = \kappa_c J_1 + (1-\kappa_c) J_2 = \frac{1}{2}\kappa_c \boldsymbol{u}_d^{\mathrm{T}} \boldsymbol{H} \boldsymbol{u}_d + (1-\kappa_c)\boldsymbol{G}^{\mathrm{T}} \boldsymbol{u}_d \tag{41}$$

where J denotes the overall allocation cost and $\kappa_c \in [0,1]$ is the coordination coefficient used to balance handling stability against motor economy. When $\kappa_c > 0$, the Hessian matrix $\kappa_c \boldsymbol{H}$ remains positive definite. Therefore, the optimization criterion is strictly convex, ensuring that a unique global optimum exists.

4.1.3 Constraints

The equality constraint is the moment balance condition:

$$\boldsymbol{B}_d \boldsymbol{u}_d = \boldsymbol{v}_d \tag{42}$$

The inequality constraints are imposed by the motor output capability and the available tire–road adhesion.

First, the torque command of each wheel must remain within the output range of its in-wheel motor. Thus,

$$-T_{i\max} \le T_i \le T_{i\max} \tag{43}$$

where $T_{i\max}$ is the maximum output torque of the i-th in-wheel motor at the current speed, determined by Eq. (10).

The road adhesion constraint limits the torque of each wheel so that it does not exceed the maximum adhesion moment that the current vertical load and road adhesion coefficient can provide:

$$-\mu R F_{zi} \le T_i \le \mu R F_{zi} \tag{44}$$

Combining the two types of inequality constraints and taking the more stringent one in each constraint, the effective lower and upper bounds of each wheel torque are defined as:

$$T_{i,\min} = \max(-\mu R F_{zi}, -T_{i\max}), T_{i,\max} = \min(\mu R F_{zi}, T_{i\max}) \tag{45}$$

where $T_{i,\min}$ and $T_{i,\max}$ denote the lower and upper effective torque limits for the i-th wheel, respectively.

Finally, the wheel-torque allocation task is formulated as the following constrained quadratic program:

$$\min J = \frac{1}{2}\kappa_c \boldsymbol{u}_d^{\mathrm{T}} \boldsymbol{H} \boldsymbol{u}_d + (1-\kappa_c)\boldsymbol{G}^{\mathrm{T}} \boldsymbol{u}_d \tag{46}$$

$$\text{s.t.} \quad \boldsymbol{B}_d \boldsymbol{u}_d = \boldsymbol{v}_d \tag{47}$$

$$\boldsymbol{u}_{\min} \le \boldsymbol{u}_d \le \boldsymbol{u}_{\max} \tag{48}$$

where $\boldsymbol{u}_{\min} = [T_{fl,\min}, T_{fr,\min}, T_{rl,\min}, T_{rr,\min}]^{\mathrm{T}}$ is the torque lower-bound vector; and $\boldsymbol{u}_{\max} = [T_{fl,\max}, T_{fr,\max}, T_{rl,\max}, T_{rr,\max}]^{\mathrm{T}}$ is the torque upper-bound vector. This problem is a small-scale strictly convex quadratic program with only four decision variables, has a unique global optimal solution, and can be reliably solved within the millisecond-level control period of the vehicle control system using the mature primal–dual interior-point method.

4.1.4 Adaptive weight adjustment mechanism

According to the mathematical boundary of the stable region in the $\beta - \dot{\beta}$ phase plane, the vehicle operating condition is classified into stable and unstable regions. The stable-region boundary divided by the double straight lines is rewritten as:

$$|\ \dot{\beta} + \bar{K}_1 A^*(\beta - \Delta d)| = \bar{K}_2 B^* \tag{49}$$

where $\dot{\beta}$ denotes the sideslip-angle variation rate; β represents the vehicle sideslip angle; A^* is the magnitude of the stable-boundary slope under standard road conditions; B^* is the intercept (half-width) of the stable-region boundary under standard road conditions; $\bar{K}_1$ is the multiplier of the slope absolute-value change caused by changes in tire–road adhesion; $\bar{K}_2$ is the multiplier of the intercept change resulting from variations in the tire–road adhesion coefficient; and Δd represents the horizontal displacement of the stable-region boundary induced by changes in the front-wheel steering angle.

Let point S represent the instantaneous vehicle operating state; d denotes the perpendicular distance between S and the stability-region centerline; d_s represents the spacing between the unstable-region boundary and the stability-region centerline; and d_x denotes the perpendicular distance between the coordination-region boundary and this centerline. From the geometric relationship in the phase plane, the distance d from point S to the center line of the stability region is:

$$d = \frac{|\bar{K}_1 A^*(\beta_0 - \Delta d) + \dot{\beta}_0|}{\sqrt{1 + (\bar{K}_1 A^*)^2}} \tag{50}$$

where β_0 denotes the current vehicle sideslip angle, and $\dot{\beta}_0$ represents its instantaneous rate of variation.

The perpendicular spacing between the unstable-region boundary and the stability-region centerline is:

$$d_s = \frac{|\bar{K}_2 B^*|}{\sqrt{1 + (\bar{K}_1 A^*)^2}} \tag{51}$$

The separation between the coordination-region boundary and the stability-region centerline is:

$$d_x = \xi d_s \tag{52}$$

where ξ is the boundary coefficient of the coordination region, with $\xi \in (0,1)$.

To ensure a continuous variation in the coordination coefficient and improve vehicle stability regulation, when the current vehicle state falls within the coordination region, the coordination weight coefficient κ_c is defined as:

$$\kappa_c = \frac{d - d_x}{d_s - d_x} = \frac{|K_1 \bar{A}^* (\beta_0 - \Delta d) + \dot{\beta}_0| - \xi |K_2 \bar{B}^*|}{(1-\xi)|K_2 \bar{B}^*|} \tag{53}$$

In summary, the coordination control coefficient can be expressed as:

$$\kappa_c = \begin{cases} 0, & d \le d_x \\ \dfrac{|K_1 \bar{A}^* (\beta_0 - \Delta d) + \dot{\beta}_0| - \xi |K_2 \bar{B}^*|}{(1-\xi)|K_2 \bar{B}^*|}, & d_x < d < d_s \\ 1, & d > d_s \end{cases} \tag{54}$$

When $\kappa_c = 0$, the vehicle state lies within the stable region, only the linear motor-loss term is retained in the objective function, and energy efficiency becomes the principal goal of torque distribution; when $\kappa_c = 1$, the vehicle is in the unstable region, the objective function retains only the quadratic tire-adhesion-utilization term, and the torque distribution aims at maximizing the stability margin; when κ_c transitions continuously between 0 and 1, the vehicle is in the coordination region, and stability and economy are coordinated proportionally. This continuous weight-switching mechanism based on phase-plane distance avoids torque jumps caused by hard switching and ensures the smoothness of the control output.

4.2 Anti-Slip Regulation

Under ideal road conditions, the four-wheel torque commands output by the optimal torque distribution module can account for both stability and economy. However, when the vehicle operates on a low-adhesion or split-μ road, some driving wheels may experience excessive slip due to insufficient road adhesion, resulting in the driving force not being effectively transmitted and even inducing vehicle instability. To this end, this paper sets an Anti-Slip Regulation (ASR) module after torque distribution as the final execution protection link of the lower-layer controller. It is worth noting that the road-adhesion constraint in the optimal torque distribution module is determined using the estimated road-adhesion coefficient μ; when this estimated value has a deviation or the road conditions change abruptly, the distribution result may exceed the actual adhesion limit. The anti-slip regulation module provides real-time closed-loop protection by directly monitoring the wheel slip state, without relying on the prior estimate of μ, thereby compensating for the inadequacy of the static constraint under dynamic operating conditions.

4.2.1 Definition and estimation of slip ratio

Under the driving condition, the longitudinal slip ratio of the i-th wheel is formulated as:

$$s_i = \frac{R\omega_i - v_{w,i}}{\max(R\omega_i, \varepsilon_v)} \tag{55}$$

where s_i denotes the slip ratio of the i-th wheel, with $s_i \in [0,1)$; R is the effective rolling radius of that wheel; ω_i denotes the rotational speed of the i-th wheel; $v_{w,i}$ represents the longitudinal velocity at the center of the i-th wheel along the wheel's longitudinal direction; and ε_v is a small positive number (taken as $\varepsilon_v = 0.1\text{m/s}$ in this paper) used to prevent numerical singularity under low-speed conditions. $s_i = 0$ indicates that the wheel is in pure rolling; a larger s_i indicates more severe slip; and $s_i \to 1$ indicates that the wheel is close to spinning.

The longitudinal velocity at the center of each wheel can be approximately calculated from the vehicle longitudinal velocity v and the yaw rate γ as:

$$\begin{cases} v_{w,fl} = v - \dfrac{c}{2}\gamma, & v_{w,fr} = v + \dfrac{c}{2}\gamma \\ v_{w,rl} = v - \dfrac{c}{2}\gamma, & v_{w,rr} = v + \dfrac{c}{2}\gamma \end{cases} \tag{56}$$

where c denotes the vehicle track width. This approximation neglects the influence of the lateral velocity component induced by the sideslip angle at the wheel center, while maintaining adequate accuracy under normal driving conditions where β is small.

4.2.2 Anti-slip control strategy

From the tire longitudinal-force–slip-ratio characteristic curve, i.e., the $\mu - s$ curve, the tire longitudinal adhesion coefficient reaches its peak at the optimum slip ratio s_{opt}, generally between 0.10 and 0.20, and beyond this value the adhesion coefficient drops rapidly and the tire enters the unstable slip region. The core aim of anti-slip regulation is to maintain the slip ratio of each driven wheel close to s_{opt} , prevent the tire from entering the unstable-slip region, and ensure effective transmission of the driving force.

To avoid frequent activation and deactivation of the controller near the slip-ratio threshold, hysteresis logic is adopted to determine the activation state of the anti-slip control. An activation threshold s_{on} and a deactivation threshold s_{off} are set, satisfying $s_{off} < s_{opt} < s_{on}$, and the anti-slip control activation flag φ_i corresponding to the i -th wheel can be written as:

$$\varphi_i(k) = \begin{cases} 1, & s_i(k) > s_{on} \\ 0, & s_i(k) < s_{off} \\ \varphi_i(k-1), & s_{off} \le s_i(k) \le s_{on} \end{cases} \tag{57}$$

where $\varphi_i(k) \in \{0,1\}$ is the anti-slip control activation flag of the i -th wheel at the k -th sampling instant; s_{on} is the activation threshold; and s_{off} is the deactivation threshold. The hysteresis width between s_{on} and s_{off} avoids control oscillation near the boundary.

When the anti-slip control is activated for the i -th wheel ($\varphi_i = 1$), the torque correction of that wheel is computed using a proportional–derivative (PD) control law based on the slip-ratio deviation:

$$\Delta T_{ASR,i}(k) = K_p\left[s_i(k) - s_{opt}\right] + K_d \frac{s_i(k) - s_i(k-1)}{T_s} \tag{58}$$

where $\Delta T_{ASR,i}$ is the anti-slip torque correction of the i -th wheel; $K_p > 0$ is the proportional gain; $K_d > 0$ is the derivative gain; and T_s is the control period. The proportional term provides the basic correction strength according to the deviation between the current slip ratio and the target slip ratio, and the derivative term provides anticipatory correction by monitoring the trend of the slip-ratio variation, thereby improving the rapidity of the anti-slip response and suppressing overshoot. When $\varphi_i = 0$, the wheel does not trigger anti-slip control, and $\Delta T_{ASR,i} = 0$.

4.2.3 Coaxial anti-slip coordination control

If torque reduction is performed only on the slipping wheel without corresponding compensation on the wheel on the other side of the same axle, the resulting torque imbalance across that axle will change, causing the generated corrective yaw moment to deviate from the desired value specified by the upper-layer controller and preventing the intended stability objective from being achieved.

There are two compensation schemes for this. The first keeps the overall longitudinal traction of the vehicle unchanged and transfers the torque removed from the slipping wheel to the non-slipping wheels on the same side. The second keeps the total yaw moment unchanged and simultaneously applies an equal torque reduction to the opposite wheel on the same axle as the slipping wheel. Considering that slip is mainly caused by insufficient road adhesion conditions and each wheel is already operating near its traction limit, the first scheme may cause the wheel receiving the torque to also exceed the adhesion limit and experience secondary slip; whereas the second scheme reduces the torque equally on the same axle, lowering the overall load level of that axle while maintaining the yaw moment unchanged, thereby increasing the vehicle’s stability reserve. Specifically, for the two wheels sharing the same axle, the greater of their anti-slip torque corrections is taken as the unified reduction for that axle and is applied to both wheels simultaneously, as illustrated in Figure 4. The unified reductions for the front and rear axles are defined, respectively, as:

$$\begin{aligned} \Delta T_{f,co} &= \max\left(\Delta T_{ASR,fl},\ \Delta T_{ASR,fr}\right), \\ \Delta T_{r,co} &= \max\left(\Delta T_{ASR,rl},\ \Delta T_{ASR,rr}\right) \end{aligned} \tag{59}$$

where $\Delta T_{f,co}$ denotes the common torque reduction applied to the front axle, whereas represents the corresponding reduction for the rear axle. After coaxial coordinated correction, the final torque command of each wheel is:

$$\begin{cases} T_{fl,cmd} = \max\left(0,\ T_{fl,opt} - \Delta T_{f,co}\right) \\ T_{fr,cmd} = \max\left(0,\ T_{fr,opt} - \Delta T_{f,co}\right) \\ T_{rl,cmd} = \max\left(0,\ T_{rl,opt} - \Delta T_{r,co}\right) \\ T_{rr,cmd} = \max\left(0,\ T_{rr,opt} - \Delta T_{r,co}\right) \end{cases} \tag{60}$$

where $T_{i,opt}$ denotes the torque assigned to the -th wheel by the optimal torque distribution module; and $T_{i,cmd}$ represents the corrected torque instruction delivered to the i -th in-wheel motor after anti-slip correction. The $\max(0,\cdot)$ operation ensures that no negative torque command is produced under the driving condition. Since the reductions of the two wheels on the same axle are equal, when neither wheel reaches the zero-torque lower bound, the left–right torque difference remains unchanged, i.e., $T_{fl,cmd} - T_{fr,cmd} = T_{fl,opt} - T_{fr,opt}$, and the same holds for the rear axle, thereby maintaining the contribution of each axle to the additional yaw moment unchanged.

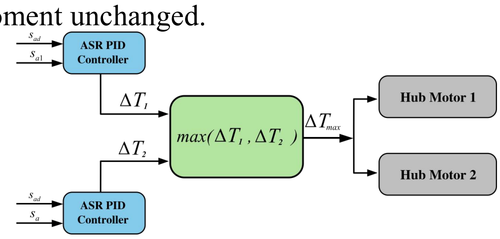

Figure 4. Structure of the Coaxial Anti-Slip Coordination Controller

5. Simulation Verification

Table 1. Table Example

Parameter	Symbol	Value
Vehicle mass	m	1580 kg
Wheelbase	L	2.67 m
Front-axle-to-CG distance	a	1.04 m
Rear-axle-to-CG distance	b	1.63 m
Track width	c	1.565 m
CG height	h_g	0.542 m
Effective wheel radius	R	0.313 m
Yaw moment of inertia	I_z	2100 $kg{\cdot}m^2$

To verify the effectiveness of the hierarchical control framework developed in this study, a co-simulation platform is established based on PanoSim and MWorks. Sysplorer. The supervisory MPC stability controller and the lower-level optimized torque allocation module are implemented in MWorks. Sysplorer, the full vehicle dynamics model adopts a four-wheel independently actuated electric vehicle model in PanoSim, and information exchange and closed-loop control are realized through the co-simulation interface between PanoSim and MWorks. Sysplorer. The full vehicle parameters used in the simulation are listed in Table 1.

To comprehensively verify the performance of the proposed method under different driving conditions, two typical simulation scenarios are designed: a double-lane-change maneuver on a high-adhesion road and a double-lane-change maneuver on a low-adhesion road.

5.1 Scenario 1: Double-lane-change Test under High-Adhesion Conditions

For this test, the tire–road adhesion coefficient is specified as 0.8, while the vehicle performs the double-lane-change maneuver at an initial velocity of 100 km/h. In this case, the tires are far from the adhesion limit, and the vehicle operating point remains inside the stable region of the phase plane. The main purpose is to evaluate the yaw-rate tracking accuracy achieved by the supervisory MPC controller and the effect of adaptive weighting in the lower-level wheel-torque allocation in reducing motor energy loss while accounting for stability. For sufficient comparison, the following three control strategies are set to participate in the simulation simultaneously. Strategy 1 is the uniform distribution scheme, i.e., the requested longitudinal force and corrective yaw moment generated by the supervisory MPC controller are allocated evenly among the four wheels without any optimization. Strategy 2 is the stability-only optimization distribution scheme, i.e., the distribution weight coefficient κ_c is fixed at 1, and the distribution objective considers only the minimization of tire adhesion utilization without considering motor loss. Strategy 3 corresponds to the complete control framework developed in this study, i.e., the phase-plane-based adaptive weight is used to dynamically coordinate between tire adhesion utilization and motor power loss. The three strategies share the same upper-layer MPC controller, and the difference lies only in the lower-layer distribution link.

5.1.1 Analysis of vehicle trajectory

Figure 5 compares the vehicle trajectories obtained using the three strategies. The results indicate that all three strategies can accurately follow the desired path on the high-adhesion road, with the lateral deviation controlled within a small range, indicating that the upper-layer MPC controller has good path-tracking capability under normal operating conditions.

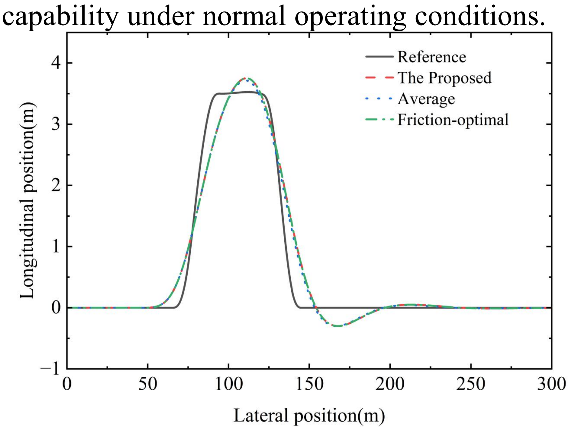

Figure 5. Vehicle Trajectory in Scenario 1

5.1.2 Analysis of yaw-rate tracking

Figure 6 shows the yaw-rate tracking performance. The yaw-rate responses obtained with all three strategies closely follow the reference signal, with very small peak tracking errors, indicating that under high-adhesion conditions the upper-layer MPC controller provides sufficient protection of yaw stability, while the selected torque allocation strategy has only a minor effect on the supervisory control performance.

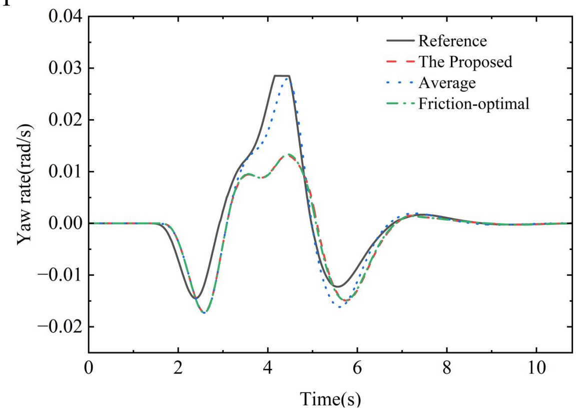

Figure 6. Yaw Rate in Scenario 1

5.1.3 Analysis of sideslip angle

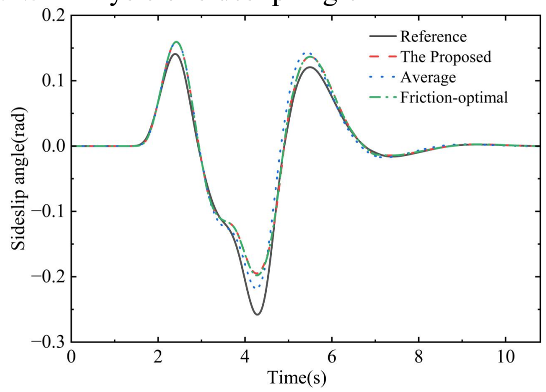

Figure 7. Sideslip Angle in Scenario 1

Figure 7 presents the sideslip-angle responses. The sideslip angles of all three strategies are maintained at a low level, and the vehicle continues to operate inside the linear stability region, further confirming the large safety margin of vehicle operation under high-adhesion conditions.

5.1.4 Analysis of phase-plane trajectory and weight coefficient

Figure 8 shows the vehicle-state path in the phase plane and the corresponding evolution of the weighting coefficient κ_c. The results indicate that, during the entire double-lane-change maneuver, the vehicle state always remains within the interior of the stability domain in the phase plane, with a large margin from the unstable-region boundary. Therefore, the adaptive weight mechanism of this paper maintains κ_c at a low level, and the distribution objective is biased toward the minimization of motor power loss, reflecting the design philosophy of prioritizing economy when the safety margin is sufficient.

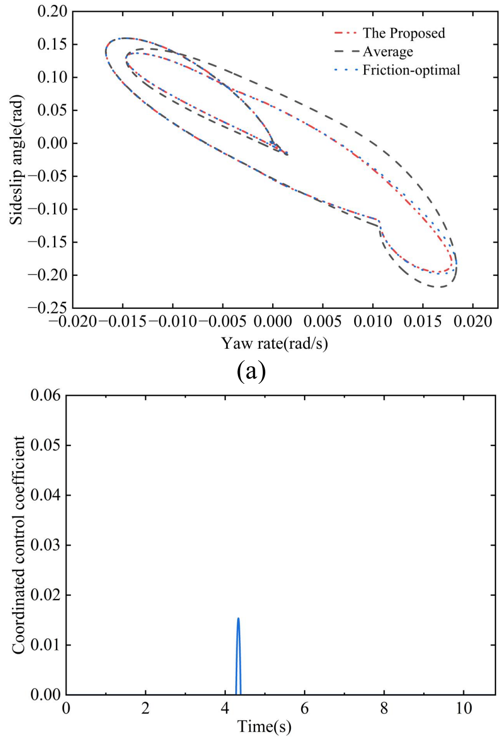

(a) (b)

Figure 8. Phase-Plane Trajectory and Coordination Control Coefficient Variation Curves in Scenario 1: (a) Phase-Plane Trajectory; (b) Coordination Control Coefficient

Figure 9 compares the wheel-torque allocation results. Under the uniform distribution scheme, the four-wheel torques are symmetrically distributed; the stability-only optimization scheme performs differentiated distribution according to the load and adhesion conditions of each wheel to balance the adhesion utilization of the wheels as much as possible; whereas the proposed scheme, on the basis of ensuring that the adhesion utilization is basically balanced, also considers the efficiency characteristics of each motor at its current operating point, distributing more torque to the higher-efficiency motors so as to reduce the total loss of the four motors.

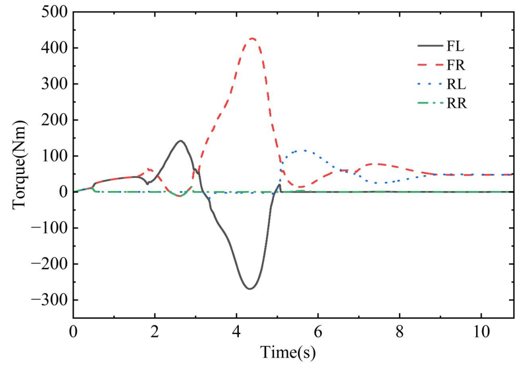

(a)

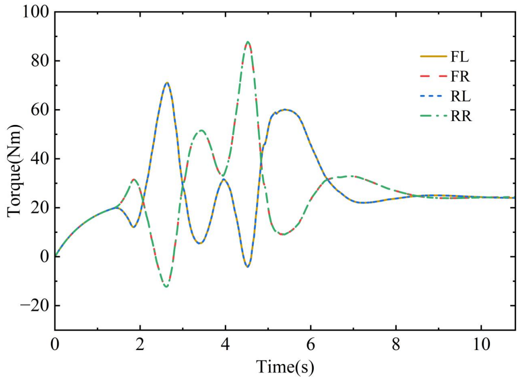

(b)

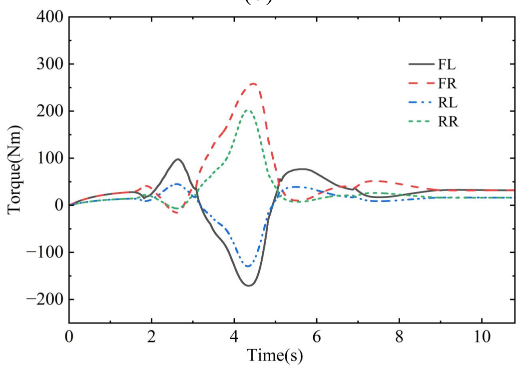

(c)

Figure 9. Torque Distribution in Scenario 1: (a) Proposed Scheme; (b) Stability-Only Optimization; (c) Uniform Distribution

5.1.5 Analysis of motor energy loss

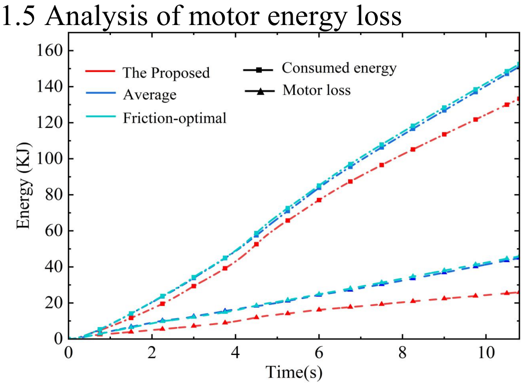

(a)

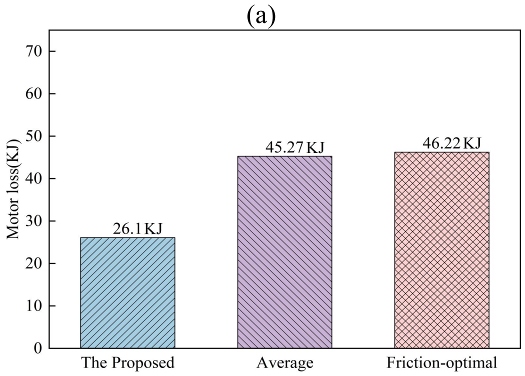

(b)

Figure 10. Motor Energy Loss in Scenario 1: (a) Time History of Total Power Loss; (b) Comparison of Cumulative Motor Energy Loss

Figure 10 shows the time history of the aggregate power dissipation of all four in-wheel motors, together with a comparison of their accumulated energy losses under the three strategies. Throughout the double-lane-change maneuver, the cumulative motor energy loss of the uniform distribution scheme is 45.27 kJ, that of the stability-only optimization scheme is 46.22 kJ, and that of the proposed scheme is 26.1 kJ. Compared with the uniform distribution scheme, the cumulative motor energy loss achieved by the proposed strategy decreases by 42.3%; relative to the stability-only optimization scheme, it is reduced by 43.5%.The reason for such a significant reduction is mainly that, under this scenario, the motors generally operate in the low- to medium-load region, where the motor efficiency is sensitive to the operating point and the gradient of the efficiency map is large; the uniform distribution and stability-only optimization schemes keep some motors operating in the low-efficiency region for a long time, whereas the proposed scheme concentrates the torque toward high-efficiency operating points and dynamically redistributes it among the four wheels, effectively avoiding operation in the low-efficiency region and thereby significantly reducing the total system loss. This indicates that, under high-adhesion normal operating conditions, the dual-objective optimal distribution method considering motor loss developed in this study effectively lowers the energy demand of the motor system without sacrificing vehicle stability, verifying the effectiveness of the energy-saving optimization.

5.2 Scenario 2: Double-Lane-Change Test under Low-Adhesion Conditions

For this scenario, the tire–road friction coefficient is reduced to 0.2 to simulate icy and snow-covered road surfaces. The test vehicle accelerates from an initial velocity of 40 km/h to 60 km/h and performs the same double-lane-change path as in Scenario 1. Under low-adhesion conditions, the tires can easily reach their available friction limit, the vehicle is at risk of instability, and the driving wheels are prone to excessive slip. This scenario aims to comprehensively verify the cooperative effect of the upper-layer MPC limit-stability control, the phase-plane adaptive weight's dynamic switching from economy to stability, and the anti-slip regulation module.

To fully demonstrate the role of each module, the following three comparison schemes are set. Scheme 1 serves as the uncontrolled baseline, i.e., no additional corrective yaw moment is applied, and the requested driving torque is equally allocated among the four wheels, and no anti-slip control is performed, serving as the baseline reference. Scheme 2 is the MPC + uniform distribution scheme, i.e., the supervisory MPC controller generates the corrective yaw moment, whereas the lower-level controller adopts equal torque allocation without the ASR module. Scheme 3 is the full control strategy developed in this study, which includes the upper-layer MPC controller, the dual-objective optimal torque distribution with phase-plane-based adaptive weights, together with the anti-slip control module.

5.2.1 Analysis of vehicle trajectory

Figure 11 compares the vehicle paths obtained under the three control schemes. Under the no-control scheme, the vehicle exhibits obvious trajectory deviation already during the first lane change, and during the second return maneuver the vehicle undergoes severe side slip and even instability, failing to complete the prescribed double-lane-change test. In Scheme 2, the supervisory MPC improves the vehicle attitude by generating a corrective yaw moment, and the trajectory-tracking effect is consequently enhanced; however, due to the lack of anti-slip control, some wheels experience excessive slip leading to driving-force loss, and the trajectory still has a certain deviation. Under the complete scheme of this paper, the vehicle can smoothly complete the full double-lane-change maneuver and achieve the best trajectory-tracking accuracy, with the lateral deviation controlled within 0.5 m.

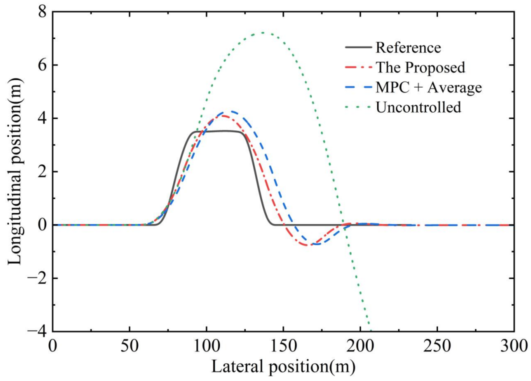

Figure 11. Vehicle Trajectory in Scenario 2

5.2.2 Analysis of yaw-rate tracking

Figure 12 shows a comparison of the yaw-rate responses. With no control applied, the yaw-rate response shows substantial oscillation and overshoot, considerably exceeding its reference, and consequently causing the vehicle to enter an unstable spinning state. The yaw-rate tracking effect of Scheme 2 is good, but there is still overshoot at the maximum lane-change demand. The complete strategy developed in this study enables the yaw rate to closely track the reference value, with the peak error controlled within 0.01 rad/s, reflecting the advantage of the coordinated operation between the supervisory MPC and lower-level optimal torque allocation.

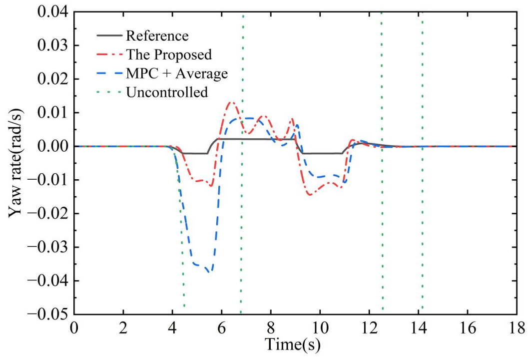

Figure 12. Yaw Rate in Scenario 2

5.2.3 Analysis of vehicle trajectory

Figure 13 compares the sideslip-angle responses obtained using the three schemes. For the uncontrolled case, its sideslip angle increases sharply to more than 12°, and the vehicle completely loses stability. Scheme 2 constrains the sideslip angle within 9°, but there is still some fluctuation. By contrast, the sideslip angle obtained with the complete strategy developed in this study remains controlled within 8°, exhibiting the best stability performance.

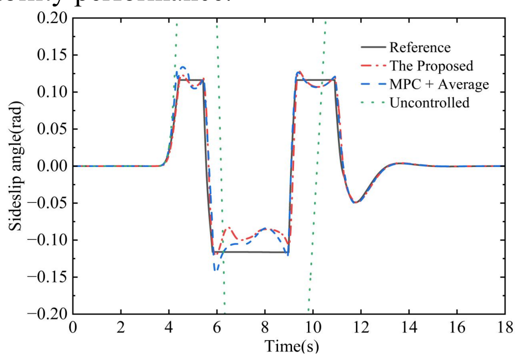

Figure 13. Sideslip Angle in Scenario 2

5.2.4 Analysis of phase-plane trajectory and weight coefficient

Figure 14 shows the vehicle-state trajectory in the phase plane and the dynamic evolution of the weight coefficient κ_c under the proposed scheme. Unlike the high-adhesion scenario, when performing a double-lane-change maneuver under low-friction conditions, the motion trajectory representing the vehicle state in the phase plane clearly approaches the boundary of the unstable region. During the lane change, when the operating state of the vehicle enters the coordination region, κ_c rises rapidly from its initially low value; when the state approaches the unstable-region boundary, κ_c approaches 1, and the distribution objective almost entirely shifts to the minimization of tire adhesion utilization to ensure stability. After the vehicle returns and enters the straight-line driving stage, the state gradually returns to the interior of the stable region, κ_c falls back accordingly, and the distribution objective again accounts for economy. This result clearly demonstrates the working process of the phase-plane adaptive weight mechanism dynamically adjusting the distribution strategy according to the real-time vehicle state, verifying its ability to transition smoothly between stability and economy.

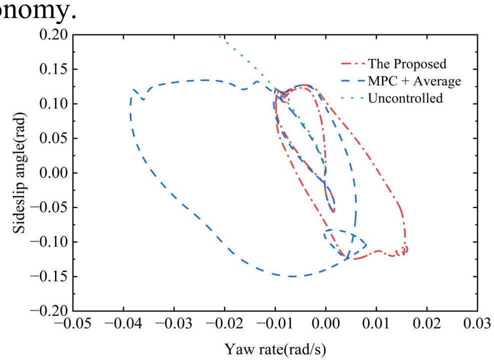

(a)

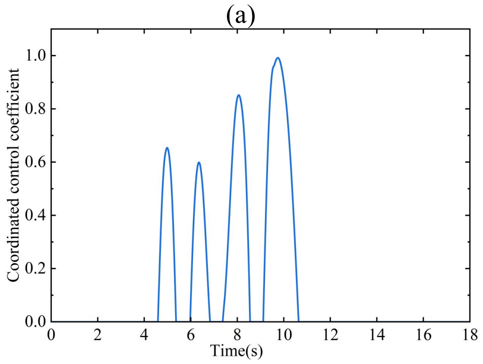

(b)

Figure 14. Phase-Plane Trajectory and Coordination Control Coefficient Variation Curves in Scenario 2: (a) Phase-Plane Trajectory; (b) Coordination Control Coefficient

5.2.5 Analysis of wheel slip ratio

Figure 15 compares the time-dependent slip-ratio responses of the four wheels. Without control, the slip ratios of several wheels exceed 0.3 or even higher during the lane change, far from the desired slip-ratio range, and the tire lateral force decays sharply, directly causing a loss of vehicle stability. Due to the absence of the ASR module, in Scheme 2 individual wheels also experience instantaneous excessive slip when outputting large torque. In the complete scheme of this paper, the anti-slip module monitors each wheel's slip condition online; when the measured wheel slip exceeds the target value of 0.1, the PD controller rapidly reduces the drive torque of that wheel and, through the coaxial equal-reduction strategy, applies an equal torque correction to the wheel on the other side of the same axle to preserve the desired yaw-moment distribution. The results presented in Figure 15 demonstrate that, with the proposed strategy, the slip ratios of all four wheels are always effectively constrained within 0.11, ensuring that the tires operate near the optimal slip ratio so that both longitudinal traction and lateral adhesion capacity can be effectively utilized.

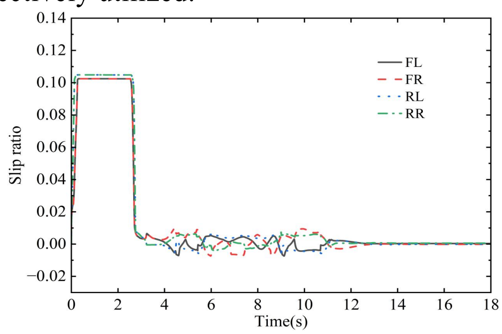

(a)

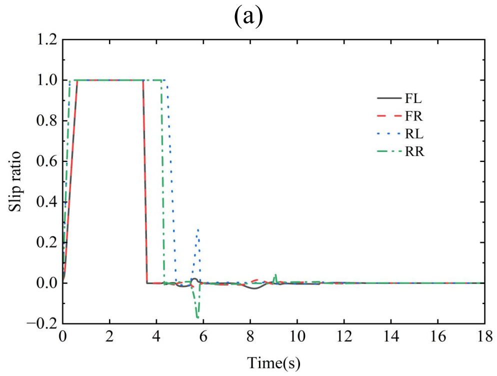

(b)

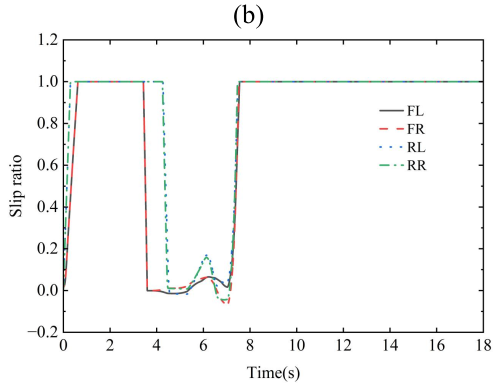

(c)

Figure 15. Wheel Slip Ratio in Scenario 2: (a) Proposed Scheme; (b) MPC + Uniform Distribution; (c) No Control

6. Conclusion

This study develops a hierarchical torque distribution coordination framework for independently driven electric vehicles that accounts for both yaw stability and in-wheel motor energy efficiency. At the supervisory level, an MPC scheme employing a 2-DOF predictive vehicle model is formulated to solve online for the corrective yaw moment needed for vehicle stabilization; at the allocation level, a convex quadratic programming model is established with tire adhesion utilization and motor energy dissipation as the two optimization objectives, and an additional phase-plane-based adaptive weight mechanism is introduced to achieve dynamic coordination between the stability and economy objectives, while an anti-slip regulation module is integrated to apply final constraints and protection to the distribution result.

The co-simulation based on PanoSim and MWorks. Sysplorer verifies the performance advantages of the developed approach. Under a high-adhesion double-lane-change test, the strategy significantly reduces the cumulative energy dissipated by the in-wheel motors while ensuring good tracking of both yaw rate and sideslip angle, reflecting its design philosophy of prioritizing economy when the safety margin remains sufficient. Under a low-adhesion double-lane-change test, the phase-plane adaptive weight mechanism can promptly switch the control focus from economy to stability and, in cooperation with the anti-slip regulation, effectively constrains the sideslip angle and keeps the slip ratio of every wheel within safe limits, thereby allowing the vehicle to successfully complete the double-lane-change maneuver that cannot be completed under the no-control scheme, indicating that the proposed strategy effectively reconciles vehicle stability with energy economy.

Future research will further investigate real-time identification of the tire–road adhesion coefficient and robust sideslip-angle estimation, and will verify them through real-vehicle tests, so as to improve the robustness and practical deployability of the developed control framework under complex real-world operating conditions.

References

[1] Gao, L. and Chai, F., "Model predictive direct motion control for distributed drive electric vehicles," IEEE Access, vol. 11, pp. 67443–67459, 2023.

[2] Tarhini, F., Talj, R. and Doumiati, M., "Dual-level control architectures for over-actuated autonomous vehicle's stability, path-tracking, and energy economy," IEEE Transactions on Intelligent Vehicles, vol. 9, no. 1, pp. 287–303, 2024.

[3] Guo, N., Zhang, X., Zou, Y., Lenzo, B., Du, G. and Zhang, T., "A supervisory control strategy of distributed drive electric vehicles for coordinating handling, lateral stability, and energy efficiency," IEEE Transactions on Transportation Electrification, vol. 7, no. 4, pp. 2488–2504, 2021.

[4] Wang, W., Ma, T., Yang, C., Zhang, Y., Li, Y. and Qie, T., "A path following lateral control scheme for four-wheel independent drive autonomous vehicle using sliding mode prediction control," IEEE Transactions on Transportation Electrification, vol. 8, no. 3, pp. 3192–3207, 2022.

[5] Lenzo, B., Zanchetta, M., Sorniotti, A., Gruber, P. and De Nijs, W., "Yaw rate and sideslip angle control through single input single output direct yaw moment control," IEEE Transactions on Control Systems Technology, vol. 29, no. 1, pp. 124–139, 2021.

[6] Peng, H., Wang, W., An, Q., Xiang, C. and Li, L., "Path tracking and direct yaw moment coordinated control based on robust MPC with the finite time horizon for autonomous independent-drive vehicles," IEEE Transactions on Vehicular Technology, vol. 69, no. 6, pp. 6053–6066, 2020.

[7] Guo, N., Lenzo, B., Zhang, X., Zou, Y., Zhai, R. and Zhang, T., "A real-time nonlinear model predictive controller for yaw motion optimization of distributed drive electric vehicles," IEEE Transactions on Vehicular Technology, vol. 69, no. 5, pp. 4935-4946, 2020.

[8] Li, C., Liu, H., Han, L., Wang, W. and Guo, C., "Multi-level coordinated yaw stability control based on sliding mode predictive control for distributed drive electric vehicles under extreme conditions," IEEE Transactions on Vehicular Technology, vol. 72, no. 1, pp. 280–296, 2023.

[9] Waqas, M. and Ioannou, P., “Automatic vehicle following under safety, comfort, and road geometry constraints,” IEEE Transactions on Intelligent Vehicles, vol. 8, no. 1, pp. 531–546, 2023.
[10] Gao, S., Wang, J., Guan, C., Zhou, Z. and Liu, Z., “Wheel torque distribution control strategy for electric vehicles dynamic performance with an electric torque vectoring drive axle,” IEEE Transactions on Transportation Electrification, vol. 10, no. 1, pp. 1692–1705, 2024.